Journal of
Applied Remote Sensing

RemoteSensing.SPIEDigitalLibrary.org

Improving hyperspectral subpixel target detection using hybrid detection space

Ruixing Li
Shahram Latifi

SPIE.

Ruixing Li, Shahram Latifi, "Improving hyperspectral subpixel target detection using hybrid detection space," *J. Appl. Remote Sens.* **12**(1), 015022 (2018), doi: 10.1117/1.JRS.12.015022.

Improving hyperspectral subpixel target detection using hybrid detection space

Ruixing Li* **and Shahram Latifi**
University of Nevada, Department of Electrical and Computer Engineering,
Las Vegas, Nevada, United States

Abstract. A hyperspectral image (HSI) has high-spectral and low-spatial resolution. As a result, most targets exist as subpixels, which pose challenges during target detection. Moreover, limitations of target and background samples always hinder the detection performance. In this study, a hybrid method for subpixel target detection of an HSI is developed. The scores of matched filter (MF) and adaptive cosine estimator (ACE) are used to construct a hybrid detection space. The reference target spectrum and background covariance matrix are improved iteratively based on the distribution property of targets, using the hybrid detection space. As the iterative process proceeds, the reference target spectra get closer to the central line, which connects the centers of the target and the background, resulting in a noticeable improvement in target detection. One synthetic dataset and two real datasets are used in the experiments. The results are evaluated based on the mean detection rate (DR), receiver operating characteristic curve, and observations of the detection results. For the synthetic experiment, the hybrid method improves more than 10 times with regard to the average DR compared with that of the traditional MF and ACE algorithms, which use N-FINDR target extraction and Reed–Xiaoli detector for background estimation. © *2018 Society of Photo-Optical Instrumentation Engineers (SPIE)* [DOI: 10.1117/1.JRS.12.015022]

Keywords: adaptive cosine estimator; background modeling; iterative improvement; low abundance target detection; matched filter; spectral variation.

Paper 170993 received Nov. 21, 2017; accepted for publication Feb. 21, 2018; published online Mar. 16, 2018.

1 Introduction

Mixed pixels, spectral variations, and calibration errors are the main challenges in hyperspectral image (HSI) target detection. Although HSI has high resolution in the spectral domain, it does not have good resolution in the spatial domain, roughly 1 to 3.6 m per pixel for aerial HSIs. Due to long distances from a scene and a low spatial resolution,[1] mixed pixels commonly exist. This complicates the target detection process.

Illumination and atmospheric variations also contribute to the uncertainty of target spectra. Spectra of the same material may vary, and different materials may show similar spectra; these phenomena are called spectral variation. Generally, researchers obtain the reference spectral curve for target detection algorithms using one of two methods, a standard spectral library or hyperspectral unmixing (HU)[2] from the data. While using a standard library in these detection algorithms, the target spectrum may deviate from the actual target being sought due to spectral variation. On the other hand, while extracting the target endmember using HU, a mismatch in estimating the number of endmembers could lead to quite different results in the extracted spectra. As most HU algorithms are based on the convex geometry assumption, the lack of full pixels of interest also leads to inaccuracy in the extracted target spectral signature. Furthermore, the original data need to be calibrated before applying the detection algorithms, and errors always happen during calibration.

*Address all correspondence to: Ruixing Li, E-mail: lir1@unlv.nevada.edu

1931-3195/2018/$25.00 © 2018 SPIE

As HSI techniques are applied to increasingly more areas, traditional target-detection methods based on a standard library or by extraction of the target spectrum using HU may still not be applicable. Furthermore, using a single spectrum extracted from the scene for target detection can cause low-detection performance due to the uncertainty of the spectra.

The proposed hybrid detection algorithm aims to detect low abundance targets (LATs) in HSI with limited target samples. First, the hybrid detection space is introduced to adopt the advantages of matched filter (MF) and adaptive cosine estimator (ACE) algorithms. As the representation of target and background are two important factors in HSI target detection, MF background estimation is introduced to improve the accuracy of the background model. Although the initial target samples are limited, the representation of the target still can be improved iteratively using the hybrid detection space, based on the statistical nature of targets.

The remainder of this paper is organized as follows. The MF and ACE target-detection algorithms are introduced in Sec. 2, and the hybrid detection algorithm proposed in this study is discussed in Sec. 3. Experimental results using both synthetic and real data are provided in Secs. 4 and 5, respectively. Conclusions are presented in Sec. 6.

2 MF and ACE Target Detection Algorithms

HSI target detection focuses on subpixel detection, which is different from detection using the more traditional high-spatial resolution images. Many algorithms have been developed for HSI target detection. The spectral angle mapper (SAM), developed by Boardman in 1993, is the simplest algorithm that is not based on any assumption of data distribution.[3,4] It has low computation cost but is not capable for subpixel target detection. The MF based on statistical distribution was proposed to improve detection performance for subpixel targets.[5] In 1995, a more powerful algorithm, the ACE,[6] was introduced to strengthen the detection performance for extremely small subpixel targets. This section reviews two statistical target-detection algorithms, the MF and ACE, which are adopted in our hybrid detection algorithm.

2.1 *Matched Filter*

MF and ACE detection algorithms, based on tested hypotheses, first, were used to formulate the target detection as a binary hypothesis test problem and then were used to estimate the likelihood ratio test (LRT) or generalized likelihood ratio test (GLRT) to perform detection.[7]

The MF model is based on the assumption that background noise has a normal distribution $N(0, C_{\mathrm{b}})$. The target also follows a normal distribution, $N(as, C_b)$, which has the same covariance statistics as that of the background but a different mean,[8] where a is the average target abundance and $s = [s_1 s_2 \ldots s_p]^T$ is the target spectral signature. For a $p \times 1$ input, x has a distribution of $x \sim N_p(as, \sigma_{\mathrm{b}}^2 C_{\mathrm{b}})$, where $a \geq 0$ and $\sigma_{\mathrm{b}}^2 \geq 0$ are scalar quantities, s is a $p \times 1$ known vector, and C_{b} is a known $p \times p$ positive definite matrix. Since the matrix C_{b} is positive definite, its square-root decomposition, $C_{\mathrm{b}}^{1/2}$, is invertible. Therefore, the whitening transformation is as follows:

$$\tilde{x} = C_{\mathrm{b}}^{-1/2} x, \qquad \tilde{s} = C_{\mathrm{b}}^{-1/2} s, \tag{1}$$

resulting in a new distribution, $\tilde{x} \sim N_p(a\tilde{s}, I)$, which is a spherical normal distribution. The new detection problem is equivalent to the original one, but it can simplify derivation and analysis.

The LRT for the whitening model leads to the MF detector:[8]

$$D_{\mathrm{MF}}(x) = \frac{\tilde{s}^T \tilde{x}}{\sqrt{\tilde{s}^T \tilde{s}}} = \frac{s^T \widehat{C}_{\mathrm{b}}^{-1} x}{\sqrt{s^T \widehat{C}_{\mathrm{b}}^{-1} s}} \gtrless_{H_0}^{H_1} \eta_{\mathrm{MF}}, \tag{2}$$

where $\widehat{C}_{\mathrm{b}}$ represents the estimated covariance matrix for the centered observation data and η_{MF} represents a threshold. D_{MF} is the projection length of the test vector onto the target vector in the whitened space. If the projection length is greater than what is typical of the background, the background hypothesis (H_0) is rejected, and the test vector is determined to contain the target.[9]

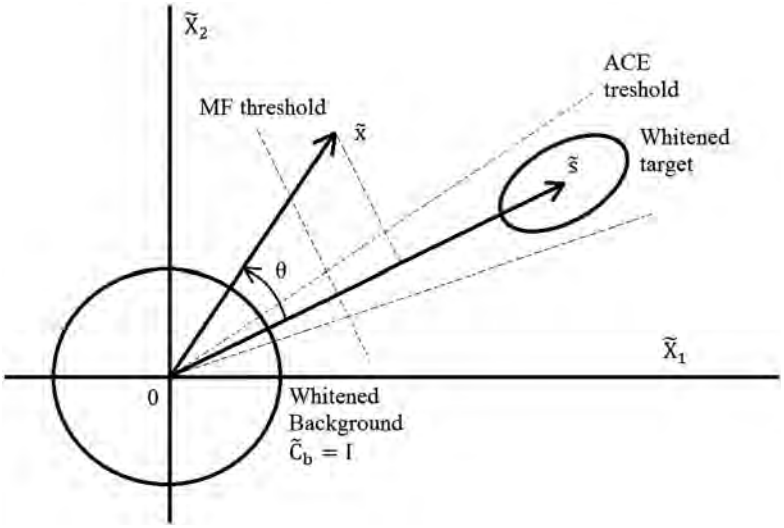

Fig. 1 Geometrical description of the MF and ACE detectors in whitened space.

2.2 *Adaptive Coherence/Cosine Estimator*

Although a and σ_b^2 are unknown in practice for MF, they can be estimated using maximum likelihood estimates:[10]

$$\hat{a} = \frac{\tilde{s}^T\tilde{x}}{\tilde{s}^T\tilde{s}} \quad \text{and} \quad \hat{\sigma}_b^2 = \tilde{x}^T\tilde{x} - \frac{(\tilde{s}^T\tilde{x})^2}{\tilde{s}^T\tilde{s}}. \tag{3}$$

Then, the GLRT can be simplified to the normalized matched filter (NMF):[11]

$$y_{\text{NMF}} = \frac{\tilde{s}^T\tilde{x}}{\sqrt{(\tilde{s}^T\tilde{s})(\tilde{x}^T\tilde{x})}} \frac{s^T\hat{C}_b^{-1}x}{\sqrt{s^T\hat{C}_b^{-1}s}\sqrt{x^T\hat{C}_b^{-1}x}} \gtrless_{H_0}^{H_1} \eta_{\text{NMF}}, \tag{4}$$

where the covariance matrix $\hat{C}_b$ is estimated from the data. The term y_{NMF}^2 is also known as the ACE.

After the whitening transformation, the estimated covariance matrix of the whitened hyperspectral background data equals the identity matrix.[7] An intuitive geometrical description of the MF and ACE detectors in the whitened space is provided in Fig. 1. The vector $\tilde{s}/\|\tilde{s}\|$, where $\|\blacksquare\|$ denotes Euclidean distance, is a unit vector, and y_{MF} is the projection distance of the observation vector onto the target. By contrast, the value of y_{NMF} is the cosine of the angle between the observation and target vector.[10] ACE assumes that only one kind of target is present in the scene and that all the subpixel targets lie in the vector that connects the background and the target signature. ACE is a measurement of how a pixel fits the mixing model, while MF is defined as the target fill fraction of a pixel.

3 Hybrid Detection Algorithm

As HSI applications become more common, future target-detection algorithms should be independent of the standard library and adaptive to spectral variation. This section introduces a hybrid HSI target detection algorithm that aims to improve low abundance subpixel target detection by gradually improving the representation of target and background. The organization of this section is as follows: Sec. 3.1 discusses the characteristics of LAT detection for MF and ACE; Sec. 3.2 introduces the MF background estimation; Sec. 3.3 defines the hybrid detection space; and Sec. 3.4 describes the hybrid detection algorithm in detail.

3.1 *Characteristics of MF and ACE in Low-Abundance Target Detection*

The whitened background and pure target are assumed to follow the normal distribution sphere. The hypersphere for the whitened dataset is defined with a radius equal to the distance from the center of the dataset to the hyperplane, which divides the dataset into 99% and 1% (Fig. 2). Subpixel targets are linear combinations of target and background, and we assume the size of these targets is sufficiently large to be statistically meaningful. The distribution region for the majority of subpixel targets should be within a trapezoid, which lies between the hyperspheres of background and pure target, and they would have a higher distribution along the central line, which connects the centers of background and target.

To evaluate the detection performance more accurately, subpixel targets within the background hypersphere are defined as low-abundance targets (LATs) and those outside the hypersphere are defined as high-abundance targets. Normally, LATs would have an abundance of less than 10% and high-abundance targets would have an abundance of greater than 10%. The detection performance for subpixel target highly relies on the number of effective bands. As most of current HSIs are with bands of 100 to 300, for those targets with fill fractions of less than 1%, the targets would fall near the center of the background and are extremely difficult to differentiate from the background. As the energy of those targets is very small, they can be considered background to simplify the detection process. The proposed hybrid method aims to improve the detection performance for LATs that have abundance values ranging from 1% to 10%.

For the sake of analysis of the detection characteristics of different methods, false-alarm rates (FARs) greater than 1% are called high FARs and less than 0.1% are called low FARs. According to Sec. 2, the detection region of ACE in the high dimensional whitened space is a hypercone and the detection boundary of MF is a hyperplane. Generally, high-abundance targets fall outside the hypersphere and most likely fall inside the hypercone even at a low FAR as the angle between high abundance targets is very small. That is to say, both the MF and ACE methods have excellent detection performance on high-abundance targets. If one method can work well on LATs, it should work well for high-abundance targets and should improve the overall detection performance. However, LATs are more likely mixed in with the background and are hard to detect.

Figure 3 shows the detection region for MF and ACE algorithms under different FAR. For the MF method at a high FAR, most LATs can be detected, as indicated to the right of the vertical line FG. However, at a low FAR, the detection performance becomes poor because most of the LATs are within the radius of the hypersphere and mixed in with the background. On the other hand, the ACE method still can capture a large portion of the targets (i.e., region DBE) between the centers of the background and the reference target spectrum at low FARs achieving better performance than that of the MF method. As the FAR increases, although the detection angle increases, many LATs still fall outside the hypercone ABC. Therefore, for LATs, the ACE has better detection performance at low FARs and the MF has better detection performance at high

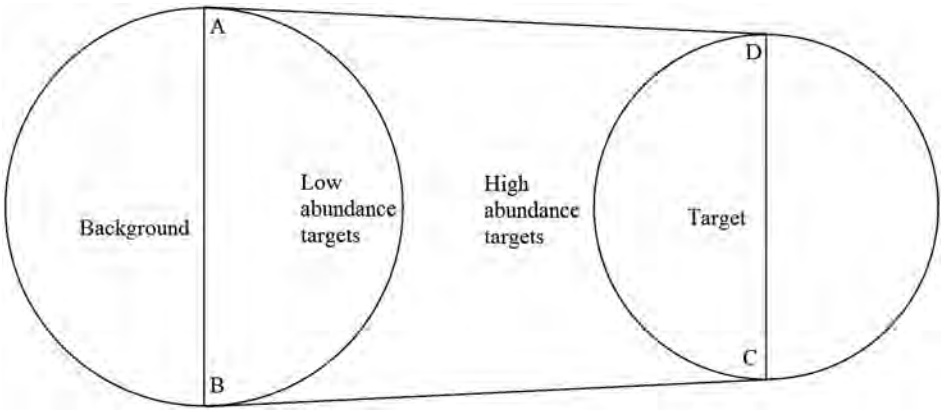

Fig. 2 Background and target distribution model. The left circle is hypersphere of background while the right circle is the hypersphere of pure target. Majority of subpixel targets are located in the trapezoid ABCD between these two circles, and LATs are located within the hypersphere of the background.

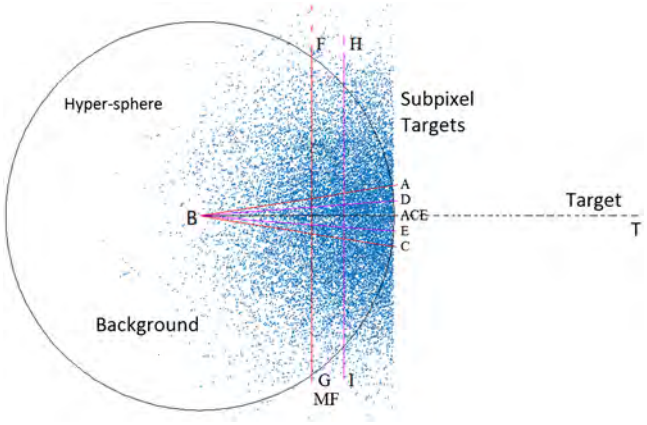

Fig. 3 Subpixel target detection inside background hypersphere. The blue points are LATs, and the black circle is the border of the hypersphere in two-dimensional space. Region ABC and line FG are the decision cone/plane at a high FAR for the ACE and MF algorithms, respectively. Region DBE and line HI are the decision cone/plane at a low FAR for the ACE and MF algorithms, respectively.

FARs. Because of these characteristics, the ACE is good for capturing potentially pure target pixels and the MF is good for extracting potentially pure backgrounds.

3.2 *MF Background Estimation*

The background covariance matrix is essential when estimating the probability density functions (PDFs) of the background and target, and ultimately affects the detection results. In a classic statistical model, the estimate covariance matrix may be illconditioned due to the contamination of subpixel targets with noise as well as high correlation between bands. A considerable mismatch could be observed between these simple models and the complicated properties of a genuine HSI background. Therefore, more accurate background models should be developed to meet the needs of low-abundance subpixel target detection.[12]

The Reed–Xiaoli detector (RXD) is one of the most popular methods for hyperspectral anomaly detection and background estimation.[13] The RXD was developed to detect pixels with spectral characteristics other than background clusters with unknown spectra covariance. For a pixel $x = [x_1, x_2 \ldots x_p]^T$ with p bands, the output of RXD is as follows:

$$RX(x) = (x - \widehat{\mu}_b)^T \widehat{C}_b^{-1} (x - \widehat{\mu}_b), \tag{5}$$

where $\widehat{\mu}_b$ is the estimated mean vector of the background and $\widehat{C}_b$ is the global background covariance matrix. Any pixel with a score greater than a certain threshold (i.e., above the red line in Fig. 4) is considered an outlier; otherwise, it belongs to the background. The RXD covariance matrix is then calculated using the pixels that belong to the background clusters.

Although the RXD background estimation would yield better background statistics compared with the global covariance matrix, the alleged background still might contain some LATs because the signals of LATs are too small to be present as abnormalities [Fig. 5(a)]. This usually results in a poorly formed covariance matrix and affects the detection performance. The MF background estimation proposed in this study attempts to remove more LATs in the background region while estimating the background.

As discussed in Sec. 3.1, the MF algorithm has good target detection performance at a high FAR; therefore, it can exclude most of the targets from the background [Fig. 5(b)]. Moreover, as the whitened background would follow the normal distribution sphere, the distribution of the MF scores for the background should be symmetrical about 0, and then the MF threshold for a certain FAR can be approximately determined by observing the distribution of pixels with MF scores less than zero. In the MF background estimation, pixels with MF scores less than 1% FAR threshold are considered the background. As the remaining targets in the background only

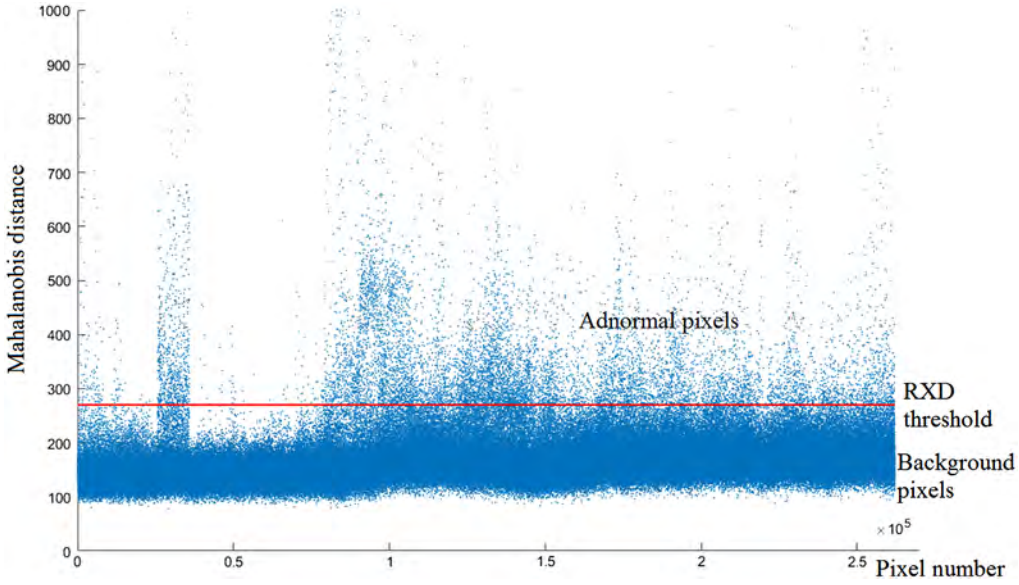

Fig. 4 Estimation of the background using the RXD. Abnormal pixels are above the threshold (i.e., the red line).

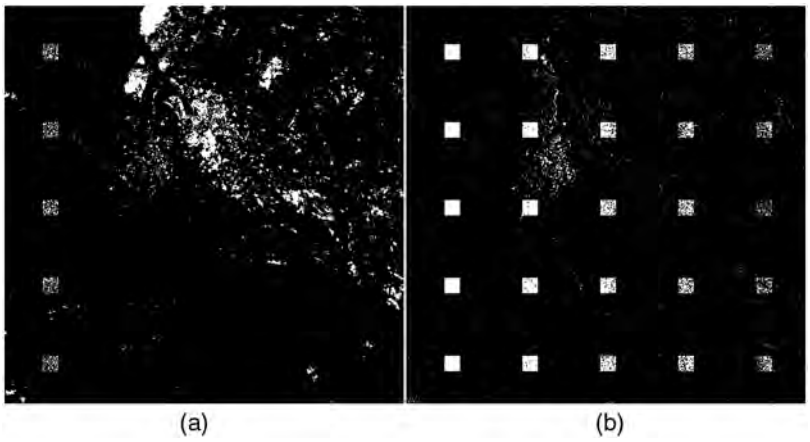

Fig. 5 Background estimation using (a) the RXD method compared with (b) the MF method. Targets are present as 25 square panels, and the right four columns are LATs. As seen in this figure, the MF method can exclude more targets from the background.

have small fractions or are of low intensity, it is assumed that the background is close to being a target-free background. MF background estimation generates a better covariance matrix and achieves more accurate PDF for the background.

3.3 *Hybrid Detection Space*

As the MF and ACE have different advantages in detecting the LATs, the hybrid detection space (Fig. 6), which is constructed by scores from the MF (x axis) and ACE (y axis), is proposed to combine these two HSI detection algorithms and thus improve the overall detection performance.

The hybrid detection space transforms high-dimensional whitened data to a visual form using the distance (MF) and angle (ACE), which are two basic elements in geometry. With some experiments on several datasets, we found that setting the FAR threshold to 1% for MF background estimation can exclude most of the subpixel targets from the background while keeping

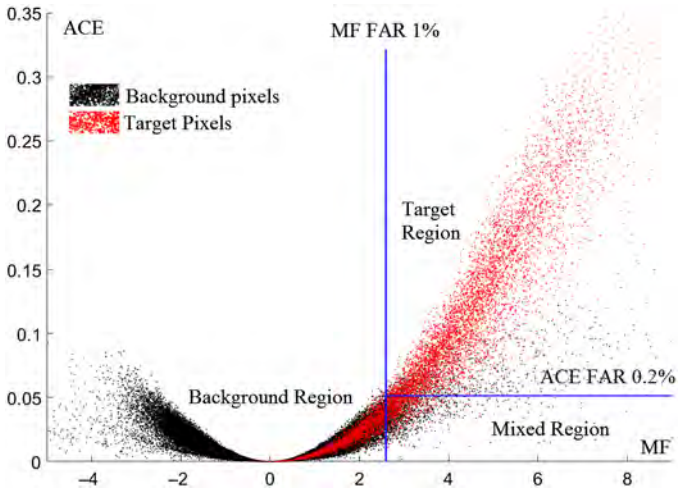

Fig. 6 An example of target and background pixel distribution in hybrid detection space. The upper-right corner is the target region and the left side is the background region. The hybrid detection space transforms the high dimensional data to a visual form. Background pixels are constrained to a small region with higher density while the target pixels expand to a large region in the first quadrant.

the majority of the background pixels. For the target subset, 0.2% is an acceptable ACE FAR threshold for our experiment datasets, which would not lead to deviation of the target spectrum while keeping a reasonable coverage rate in the hybrid algorithm. Therefore, the region with MF FARs greater than 1% is considered the background (i.e., the area to the left of the black line of Fig. 6). The region with ACE FARs less than 0.2% and MF FARs less than 1% is considered the target region (upper right corner). The region in the lower right corner is defined as the mixed region.

In a p-dimensional space, the whitened background is assumed to follow a normal distribution sphere, $N_p(0, I)$. For a constant p and a constant FAR, the ACE score/angle of the hypercone is constant. This is the same for MF/distance from the hyperplane to the center of the background. For example, for an HSI of 172 bands, the ACE score is ∼0.06 at 0.2% FAR and the MF score is ∼2.7 at 1% FAR. This indicates that most of the background would be confined in a small background region in the hybrid detection space. High-abundance targets located in the target region are far from the background region. The corresponding location in hybrid detection space for a certain pixel can be used to determine whether it is the target; this helps in analyzing the data and separating the target from the background.

As the whitened background follows the normal distribution sphere in high-dimensional space, the center of the background with the highest density is transformed to the origin of the hybrid detection space, and the background distribution in the hybrid detection space is symmetrical about the y axis. If some targets are present, the pixel distribution in the hybrid detection space performs asymmetrically about the y axis. As targets would fall in the first quadrant (with filled fraction greater than 0), the pixels in the second quadrant could be considered pure background. The corresponding threshold for a certain FAR can be estimated by observing the pixel distribution in the second quadrant. This helps to set thresholds for separating the target and background.

3.4 *Hybrid Detection Algorithm*

We have introduced MF background estimation to improve the description of the background in Sec. 3.2. We also introduced an intuitive geometric description for the distribution of background and target pixels in Sec. 3.3, which enhances the separability of target and background. However, the reference target spectrum used in ACE and MF would also affect the detection performance greatly. Describing the target with limited training samples is always a great challenge in HSI target classification/detection.[14,15] We proposed our hybrid detection algorithm to gradually

Algorithm 1 Hybrid detection algorithm.

Initialization:

1. Pick three to five high-abundance target pixel(s) from the image, and average them to get an initial reference target spectrum.
2. Perform the MF and ACE detection algorithms, using the initial target spectrum and global covariance matrix. Use the scores of MF and ACE to construct the hybrid detection space.

Main iteration:

3. In the hybrid detection space, consider as targets all pixels with ACE FARs less than 0.2% (0.01% for the first and second iterations) and MF FARs less than 1%.
4. Average the targets to update the reference target spectrum, $\mathrm{sp}(i)$.
5. Use the region with MF FARs greater than 1%, assumed to be the background, to calculate the respective covariance matrix $C_b(i)$.
6. Use the new reference target spectrum $\mathrm{sp}(i)$ and the background covariance matrix $C_{\mathrm{b}}(i)$ to perform the MF and ACE algorithms and update the pixel distribution in the hybrid detection space.
7. Calculate the evaluation metrics: N_i and L_i.

Stop the main iteration if $N_i/N_{i-1} < 1.02$ or $L_i/L_{i-1} < 1.02$; **else**, go to Step 3,

8. Follow the detection order from the high ACE score to the low ACE score in the target and mixed region first, then from the high MF score to the low MF score in the background region.

improve the representation of the target based on the distribution nature of targets and the hybrid detection space. As the initial target spectra of hybrid detection algorithm are randomly picked from the image, our method is generally applicable to most HSI target detection scenarios if there are sufficient target pixels in the image.

The proposed hybrid detection Algorithm 1 is as follows.

In HSI, both the background and the target are assumed to follow multivariate normal distribution, and subpixel targets are the linear combinations of the background and target subsets. Therefore, as shown in Fig. 7, subpixel targets would have a greater density along central Line BT, which connects the centers of the background and the target.

To achieve better detection performance, the reference target spectrum must be close to line BT so that the detection region can cover more targets. However, for a randomly picked spectrum, it may fall far away from line BT, for example, sp1. As a result, the ACE detection area only can cover a region (ABC) with a low-density target distribution.

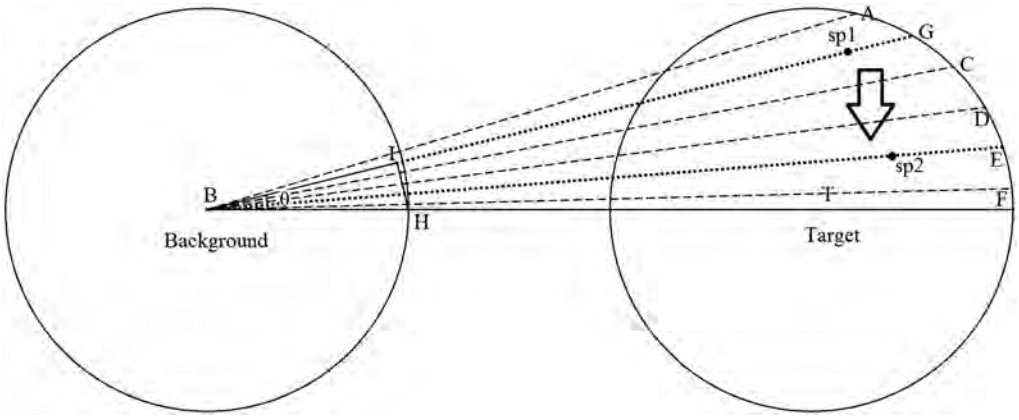

Fig. 7 Terminal condition I: maximum target coverage. As the reference target spectrum gets very close to the central line BT, the ACE detection hypercone can cover a maximum number of detected targets, and the iterative process should be terminated.

In the hybrid algorithm, first, a few high-abundance target pixels are selected randomly from the image and averaged to get an initial reference target spectrum. Then, the MF and ACE detection algorithms are applied to the data using a global covariance matrix. The scores of MF and ACE are used to construct the hybrid detection space. Normally, an ACE FAR threshold for the target region is set as 0.2%. However, in this study, it is necessary to set the target region with an ACE FAR threshold of 0.01% for the first two iterations because the target subset is very small at the beginning. A high FAR threshold brings more background pixels into the target subset and reduces the accuracy of detection.

At this point, a new background covariance matrix is evaluated from the new background subset, and a new reference target spectrum is calculated by averaging all the pixels in the target region. If the target spectrum is noticeably different from those of the background clusters, the target and background distributions are similar to those shown in Fig. 7. In the detection region ABC, region GBC was closer to the line BT than region ABG and thus would have higher target distribution. As a result, the next reference target spectrum, sp2, would be closer to line BT than sp1 would be.

When applying sp2 as the reference target spectrum, most of the targets have higher ACE and MF scores and thus would escape from the background region in the hybrid detection space. As a result, more target pixels can be detected at a specific FAR. For example, if point H in line BT is the pixel to be tested, then, as the reference target spectrum moves from sp1 to T, the ACE score increases from $\cos(\theta)$ to 1, and point H escapes from the background region. As a result, the new background would be purer than the previous one. After a few iterations, the reference target spectrum falls on or very close to line BT. Theoretically, the number of pixels covered by the hypercone outside the hypersphere, N_i (where i is the number of iterations)—which includes the detected targets and some constant false alarms of the background—would reach a maximum value, at which point the iteration process should be terminated.

To achieve better detection performance in this study, the purity of target subset needs to be ensured. If some abnormalities (sp2) with similar spectra as the target (sp1) are present, as shown in Fig. 8(b), the detection region of MF algorithm may be contaminated by other abnormalities. On the other hand, the hypercone of ACE only covers a small region around the targets while using 0.2% FAR. This would ensure the purity of the target samples; therefore, the ACE was selected to determine the target subset.

If abnormalities similar to the target are present, then the iterative process may deviate from the target spectrum to other abnormalities because the transition region also may have higher pixel density than the actual target region. Therefore, a new metric, the maximum MF score (Fig. 9), is needed to improve the accuracy of the hybrid method.

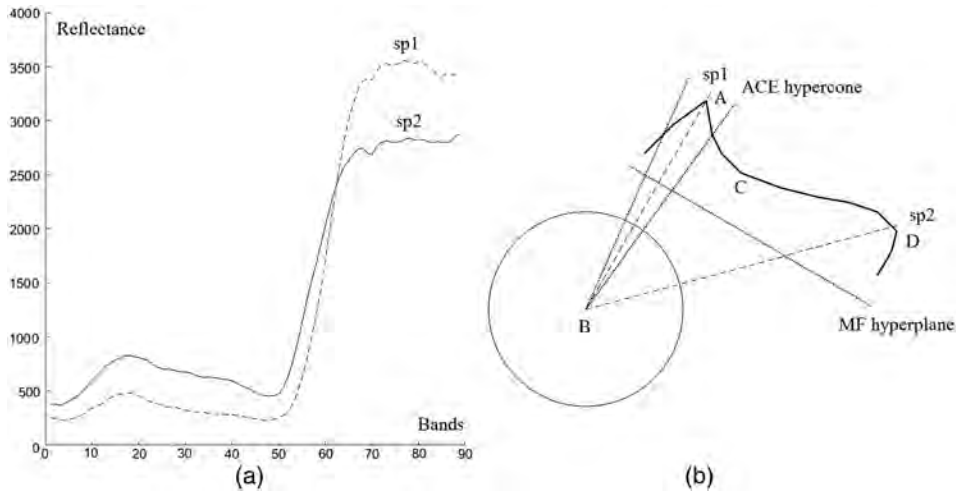

Fig. 8 Abnormalities with a similar spectrum to the target are present for (a) the target spectrum, sp1, and an abnormality having a similar spectrum, sp2; and (b) targets, similar abnormalities, and the background distribution in whitened space.

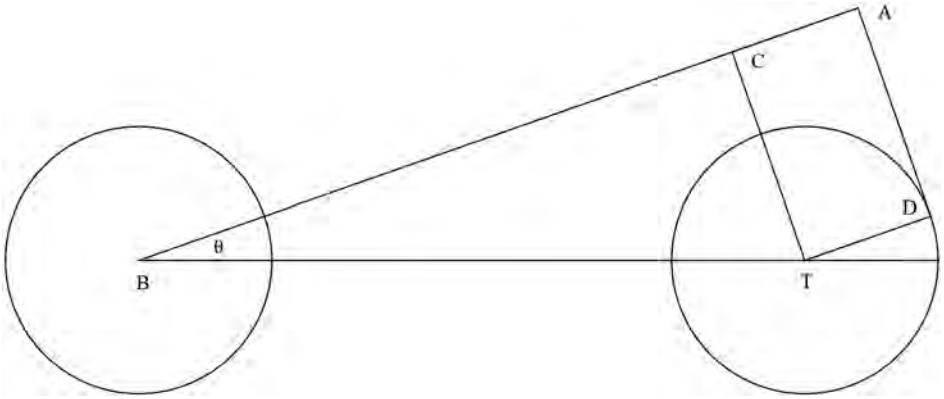

Fig. 9 Terminal condition II: maximum MF score. As the reference target spectrum gets very close to the central line BT, the average of top 100 MF scores would reach a maximum value, and the iterative process should be terminated.

In Fig. 9, points B and T are the centers of the background and target, respectively, and A is the reference target spectrum. The maximum MF score is the distance of BA:

$$\text{Max(MF)} = BA = BC + CA = BT \times \cos(\theta) + R_T, \tag{6}$$

where BT is the distance from T to B; θ is the angle between the reference target spectrum and the central line; and R_T is the radius of targets in whitened space. Since BT and R_T are constant, the maximum MF score increases as θ decreases. The MF score reaches a maximum value when the reference spectrum is very close to the central line.

As in the transition region, the maximum MF score usually decreases [Fig. 8(b)]; this can imply that the spectrum is moving to an abnormal region. To mitigate the effect of abnormal distribution, the top 100 MF scores are averaged as an index (denoted as L_i for i'th iteration) to determine whether the iterative process should be terminated.

The thresholds for terminal conditions are set as: $N_{i+1}/N_i < 1.02$ or $L_{i+1}/L_i < 1.02$. The iterative process should be terminated if either condition is satisfied, at which point the optimal spectrum is assumed to be achieved. These thresholds are determined based on experimental data. If the thresholds are set too high, the iterative process may stop too early and not reach the optimal results. In the iterative process, the MF background estimation can keep the background as the background and only the target can escape from the background region. This is because most of the background (99%) is located inside the background region, the

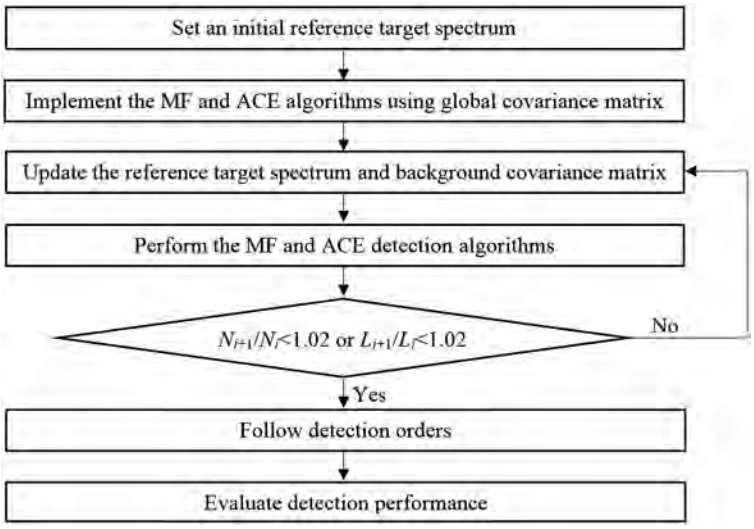

Fig. 10 Flowchart of the hybrid detection algorithm.

corresponding covariance matrix reflects the correlation between bands of background and constantly constrains the background pixels into background region. Therefore, the number of pixels inside the hypercone or maximum MF score would converge. However, in real practice, due to the error in estimating the covariance matrix, these numbers may still grow at a very slow rate after some iterations. As a result, if the threshold is set too low, it would take a long time to coverage or may even diverge. Therefore, we set the threshold as 1.02 to exclude these abnormal cases. Moreover, we can ensure that the final reference target spectrum is on or very close to the central line in this way.

Finally, the background region would have the lowest target-to-background ratio (TBR) and the target region would have the highest TBR. Avoiding the background region yields better detection performance while keeping a constant FAR. During the final step of the detection process, the detection order first should be from the high ACE score to the low ACE score in the target and mixed region. Then, as the FAR reaches 1% (and the ACE score equals 0), the next detection order should move from the high MF score to the low MF score. A flowchart of the hybrid detection algorithm is shown in Fig. 10.

4 Experiments with Synthetic Data

The effectiveness of the hybrid detection algorithm for subpixel target detection with synthetic data is described in this section, and the results are compared with those of counterpart methods.

4.1 *Experimental Model*

The original dataset for the synthetic experiment was taken from the Jet Propulsion Lab of the National Aeronautics and Space Administration (NASA/JPL),[16] collected by airborne visible/infrared imaging spectrometer (AVIRIS), which operates in the visible-to-near-infrared (VNIR) and shortwave infrared (SWIR) range of 400 to 2500 nm, and sampled to achieve 224 spectral bands. However, only 172 spectral bands were selected by discarding water absorption and noisy bands. The selected spectral bands were the 3rd to 43rd, 45th to 60th, 67th to 80th, 86th to 105th, 121st to151st, 172nd to 173rd, and 177th to 224th. This image then was cropped into the regions of interest, with a pixel size of 512×512. A target implantation strategy was applied to the original dataset.[13] First, the signatures for water were extracted from the AVIRIS data, Moffett field. Then, water spectra were implanted into the Cuprite image, using the linear mixing model (LMM).[17]

A traditional detection method (TDM) was introduced to compare the performance. First, principal component analysis (PCA)[18] transformation was performed to solve for the covariance matrix and eigenvalues. Each eigenvalue was normalized by dividing the sum of all of them. If the sum of the first n normalized eigenvalues reached a threshold of 0.999, then the number n was considered the number of endmembers. Second, the N-FINDR algorithm was performed to extract the endmembers. The extracted spectra were matched to the reference spectrum, which is the average of high-abundance target spectra known to be in the scene, using the SAM. The endmember with the minimum angle when compared with the reference spectrum was considered the target endmember. Third, the RXD algorithm was applied to evaluate the background covariance matrix. The RXD threshold was set to the value that detects the number of abnormalities approximate to the targets present in the scene. Finally, the MF and ACE detection algorithms were performed, using the extracted target endmember and the RXD estimated covariance matrix.

For the hybrid method when using synthetic data, three random target spectra from high-abundance target samples were selected. As the insertion points were known, the ground-truth image also was known. At this point, detection performance under a certain FAR was easy to calculate. Finally, the results were compared with the counterpart methods. As the performance of TDM was much worse than the hybrid method, another method—improved traditional detector (TRD), which uses the best target spectrum of the hybrid method and the RXD covariance matrix—also was applied to evaluate the effectiveness of the hybrid method. The flowchart for synthetic experiment is shown in Fig. 11.

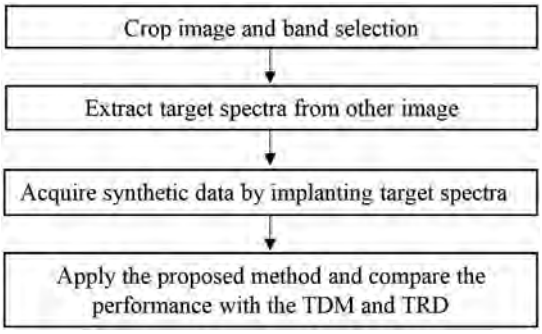

Fig. 11 Flowchart for the synthetic image experiment.

Although a synthetic image can provide a totally controllable environment to evaluate the performance of the hybrid detector, one of the main concerns was how to model it as closely as possible to a real-world image, reduce the bias, and provide meaningful results. The synthetic dataset introduced a scenario having 8000 low-abundance (1% to 3%) target pixels and 2000 high-abundance (60% to 95%) target pixels; these were presented as 25 integrated panels.

This experimental model could simulate target variations in the real world and could model the coexistence of high-abundance targets and LATs. The high-abundance targets likely are to be detected; therefore, in this experiment, the detection rate (DR) only referred to the LATs. In this way, detection performance of low-abundance subpixel targets could be evaluated more accurately than using the overall DR.

Finally, the detection performance was evaluated using receiver operating characteristic (ROC) log curves and the average DR, which are common metrics for performance evaluation.[13] Detection results under a certain FAR as well as pixel distribution in hybrid detection space also were provided to show the effectiveness of the hybrid method.

4.2 *Descriptions of Datasets*

This original image covered Cuprite Hills in Esmeralda County of southern Nevada, an area having diverse types of minerals. The synthetic dataset 1 was generated using LMM. A synthetic pixel with a spectral signature Z was the mixture of (1) the desired target T (T was a spectrum randomly selected from 3500 water signatures extracted from the Moffett field dataset) with abundance fraction a and (2) a background signature B of a selected pixel in the original image with abundance fraction $(1 - a)$, as expressed below:

$$Z = a \times T + (1 - a) \times B. \tag{7}$$

Figure 12 shows the pseudocolor image and the ground-truth map of 25 target panels for dataset 1. As shown in Fig. 12(b), this synthetic image had 5×5 target panels in different

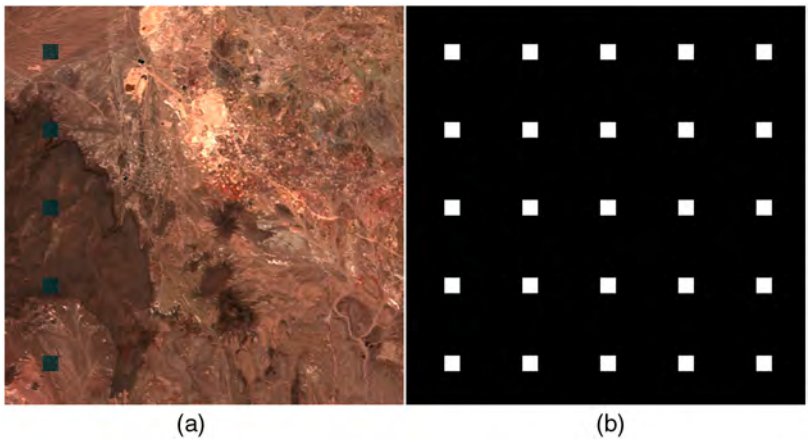

Fig. 12 (a) The pseudocolor image and (b) the ground-truth map for dataset 1.

locations. The abundance fractions of the panels reduced from left to right. The far left column had maximum values that were randomly generated, ranging from 0.6 to 0.95. The abundances for the second, third, fourth, and fifth columns were random numbers from 0.025 to 0.03, 0.02 to 0.025, 0.015 to 0.02, and 0.01 to 0.015, respectively. From Fig. 12(a), one can see that, because the abundances of the right four columns were so small, these targets could not be discerned in the RGB image.

4.3 *Experimental Results and Discussion*

Figure 13 shows the iterative improvement of the reference target spectrum. This image transformed high-dimensional data into a two-dimensional data plot, using PCA. In this figure, B is the center of the background; T is the center of the target; black dots are background pixels; green dots are target pixels; and sp, sp1, sp2, and sp3 are the reference spectra acquired when using the hybrid method. The trajectory of the reference target spectra got closer and closer to the central line, BT.

From Table 1, one can see that sp2 was the best target spectrum, according to the iterative terminal conditions provided in Sec. 3.4, and had the minimum angle to line BT. The detection performance for the various reference spectra at different FARs is provided in Table 2. Of all the spectra, sp2 had the best average DR.

Target-background separability for the initial results as well as best-detection results when using the hybrid method can be seen in the hybrid detection space in Fig. 14. The black dots stand for background pixels, while the red dots stand for target pixels. The background always is constrained in a small region and is symmetrical about the y axis during the iterative process. At the beginning, the subpixel targets were mixed in with the background; however, they achieved better separability after applying the hybrid method because most of them escaped from the background region.

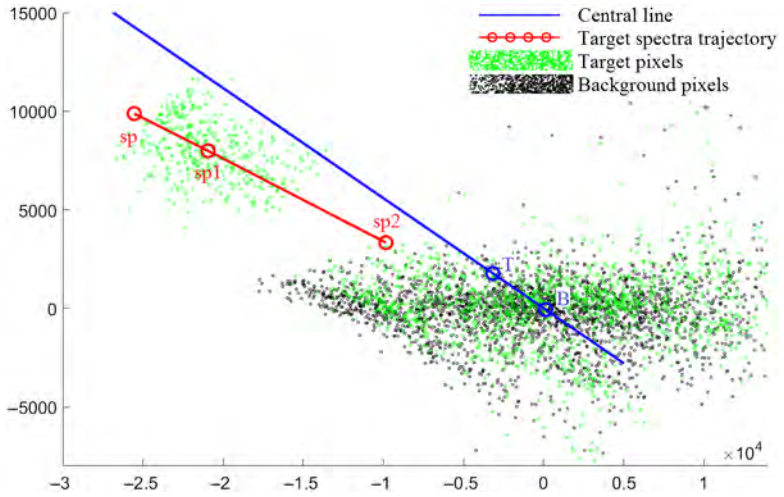

Fig. 13 Improvement in the reference target spectra for dataset 1. x-axis and y-axis are first and second principal components, respectively.

Table 1 Evaluation of spectra for dataset 1.

Reference Spectrum	Sp	sp1	sp2	sp3
Target detected	2142	7390	8302	8715
Max (MF)	15.6	158	222	226
Angle	3.610	1.192	1.012	/

Table 2 Comparison of DR under various reference target spectra for dataset 1.

Spectrum	FAR	0.02%	0.05%	0.1%	0.2%	0.5%	1%	2%	5%	Mean
Sp	MF	0	0.0006	0.0014	0.0066	0.0236	0.0414	0.0739	0.154	0.0377
	ACE	0	0.0006	0.0015	0.0029	0.0094	0.0174	0.0299	0.0696	0.0164
sp1	MF	0.023	0.1274	0.3511	0.5326	0.6975	0.7875	0.8578	0.9197	0.5371
	ACE	0.3535	0.4387	0.51	0.5751	0.659	0.7205	0.781	0.8524	0.6113
sp2	MF	0.005	0.0709	0.2285	0.4636	0.6774	0.7833	0.8576	0.9231	0.5012
	ACE	0.3602	0.4367	0.5101	0.5814	0.6794	0.7496	0.8067	0.8766	0.6251
sp3	MF	0.0014	0.0236	0.1278	0.3706	0.6362	0.7705	0.8518	0.9223	0.4630
	ACE	0.301	0.374	0.464	0.5439	0.6646	0.7426	0.807	0.8789	0.597
HDS	Fusion	0.3671	0.4456	0.5268	0.6022	0.7175	0.7833	0.8576	0.9231	0.6529

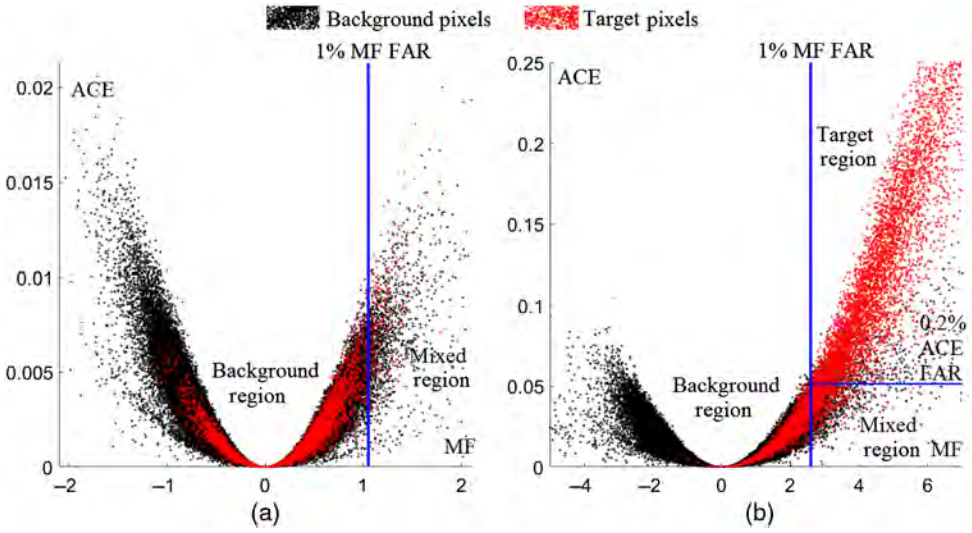

Fig. 14 Target-background separability (a) before and (b) after applying the hybrid method.

Finally, the detection performance of the hybrid method, as shown in Table 3, was compared with the TDM and TRD methods. A comparison of ROC log curves is shown in Fig. 15. Both the ROC curve and the average DR showed that the hybrid method had better performance than the TDM and TRD methods.

Figure 16 shows the detection results for the TRDM and the hybrid algorithm at 1% FAR. For high-abundance targets, both algorithms could detect all of the targets. For LATs, in Fig. 16(a), the right two columns of the targets were hardly detected. However, in Fig. 16(b), the middle three columns were almost detectable. This indicates that the detection performance of the hybrid method was much better than other counterparts for dataset 1 at 1% FAR.

The TDM, which used N-FINDR target extraction and RXD background estimation, had the worst performance due to errors in the extracted target spectra and the background statistics. Detection results for the traditional method depended greatly on the quality of the extracted target spectra. The actual target spectra may not be extracted due to a lack of full pixel targets in the scenario. Moreover, a single pixel spectrum from the scene could not reflect the spectral variation of the targets; therefore, the traditional method did not have very good performance.

Although the endmember extraction technique can be improved using such techniques as NMF, the computational cost also would increase. That the TRD method had better performance

Table 3 Detection performance of the hybrid method versus traditional methods for dataset 1.

FAR	0.02%	0.05%	0.1%	0.2%	0.5%	1%	2%	5%	Mean
TDMF[a]	0.0001	0.0006	0.0018	0.0031	0.011	0.0256	0.057	0.1411	0.0300
TDMA[b]	0	0.0004	0.0016	0.0045	0.0108	0.0209	0.0397	0.089	0.0209
TRDM[c]	0	0.003	0.0343	0.1251	0.3147	0.4427	0.5669	0.7	0.2733
TRDA[d]	0.0454	0.0833	0.1325	0.1854	0.2574	0.3049	0.3596	0.4465	0.2269
HDS[e]	0.3671	0.4456	0.5268	0.6022	0.7175	0.7833	0.8576	0.9231	0.6529

[a]TDMF = MF algorithm under TDM conditions.
[b]TDMA = ACE algorithm under TDM conditions.
[c]TRDM = MF algorithms under TRD conditions.
[d]TRDA = ACE algorithms under TRD conditions.
[e]HDS = hybrid detection space method.

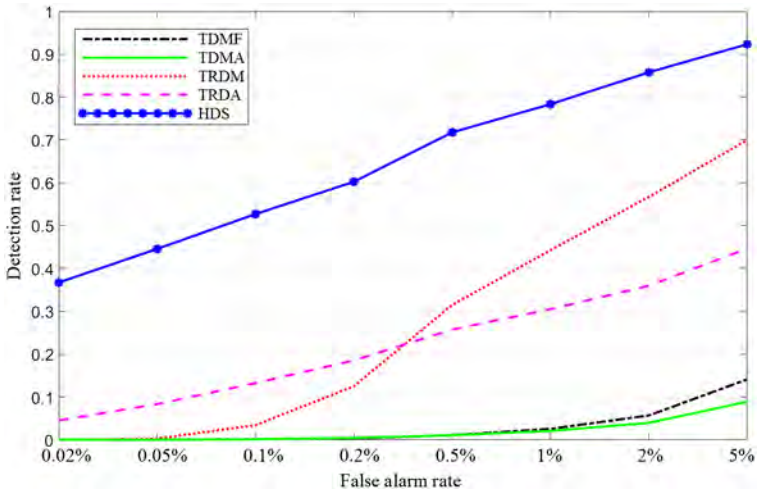

Fig. 15 Comparison of ROC curves for dataset 1. The blue line is the HDS, the red line is the TRDM, the magenta line is the TRDA, the black line is the TDMF, and the green line is the TDMA.

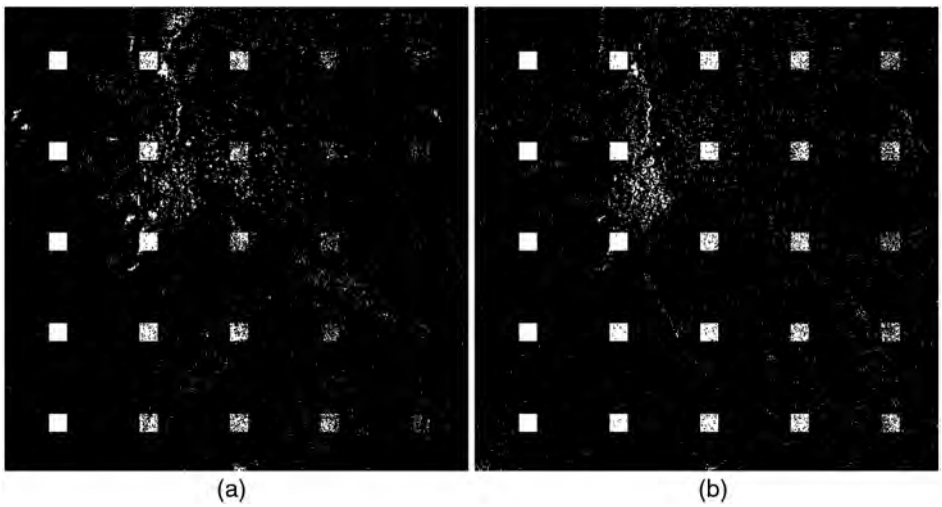

Fig. 16 Comparison of detection results of (a) the TRDM method and (b) the hybrid method for dataset 1 at 1% FAR.

than TDM implies the importance of the reference target spectrum. The fact that the hybrid method performed better than TRD indicates that MF background estimation was superior to RXD background estimation.

Due to the mismatch of extracted spectrum in the TDM method, the performance of the TRD method was much better than that of the TDM method. Therefore, only the detection results of TRD were adopted to compare with the hybrid method in the following experiments.

5 Experiments with Real Data

5.1 *Performance Evaluation for Real Datasets*

For the real datasets, because the ground-truth images for the subpixel targets were unknown, the detection results at a certain FAR for the hybrid method were compared with that of the TRD method by means of observation. It would have been better to have a high-spatial-resolution image for the real HSI datasets to determine if the detected pixels consisted of the target of interest; however, it is not easy to find such data. Because a pixel is more likely to be a target if the majority of its surrounding pixels are targets, the detection results for real-data experiments were judged by combining the contextural information of the image.

For example, if some soil pixels that are close to grass are detected as "grass," then these soil pixels would be considered to have some fill factions of grass that are too small to discern by human observation. However, the hybrid method could catch the subtle spectral variations in these pixels and could detect them as targets. Although this observation method may produce some errors, it was the best way to evaluate the hybrid method when detecting low-abundance subpixel targets of real datasets.

5.2 *Description of Datasets*

5.2.1 *Dataset 2: Moffett field*

Moffett field, located in Santa Clara County in northern California, was the launch site for the AVIRIS sensor in 1987 and has been used by NASA/JPL as a remote-sensing test site. The Moffett field image showed a very smooth area of water and a fairly homogeneous urban area that mainly consists of three components: water, soil, and vegetation.[19] The region provides an ideal study area for water variability, urban studies, and vegetation. After preprocessing, this image had a spatial dimension of 512×512 pixels, each having 172 bands with 52 of the noisiest bands removed.

5.2.2 *Dataset 3: Pavia University*

The third dataset was a Pavia University image, acquired from the University of Pavia, Italy, using a reflective optics system imaging spectrometer sensor.[20] The scene shows an urban area consisting of various buildings, parking lots, roads, and other typical human-made constructions, together with trees, green areas, and bare soil.[21] The image size in pixels is 610×340, with a spatial resolution of 1.3 m/pixel. The original image had 103 spectral channels, covering a wavelength range from 0.43 to 0.86 μm. After discarding 14 noisy spectral bands, only 89 channels were preserved for the experiment.

5.3 *Experimental Results*

5.3.1 *Dataset 2*

The Moffett field data collected by AVIRIS were used for experimental evaluation of the hybrid detector in real scenarios. Vegetation in the scene was considered the target of interest. Figure 17 shows iterative improvement of the reference target spectrum. Because the background and target truth maps were unknown, the final target region was assumed to include all

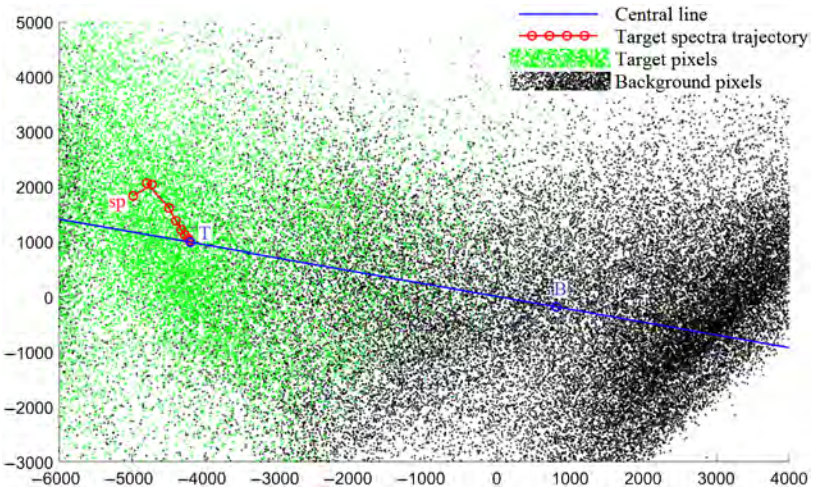

Fig. 17 Improvement in the reference target spectra for dataset 2. *x*-axis and *y*-axis are first and second principal components, respectively.

the targets, and the final background region was assumed to include all the background. At this point, the centers T and B could be calculated. Generally, the trajectory of the reference target spectra became closer and closer to the central line. As shown in Table 4, which evaluates the spectra acquired from the hybrid method, sp8 was the spectrum that satisfied the terminal conditions.

Pixel distribution in hybrid detection space for the initial and final detection results of the hybrid method is shown in Fig. 18. In Fig. 18(b), potential targets escaped from the background region. Figure 19 compares the detection results of the TRDM and hybrid method at 0.1% FAR.

Table 4 Evaluation of spectra for dataset 2.

Reference spectrum	sp	sp1	sp2	sp3	sp4	sp5	sp6	sp7	sp8	sp9
Target detected	1722	8971	15980	23171	28583	32021	34823	36352	37499	37261
Max (MF)	5.1	9.3	13.8	17	19.7	21.3	22.9	23.9	24.6	24.3
Angle	46.21	21.49	15.28	8.78	5.15	2.95	1.67	0.663	0	/

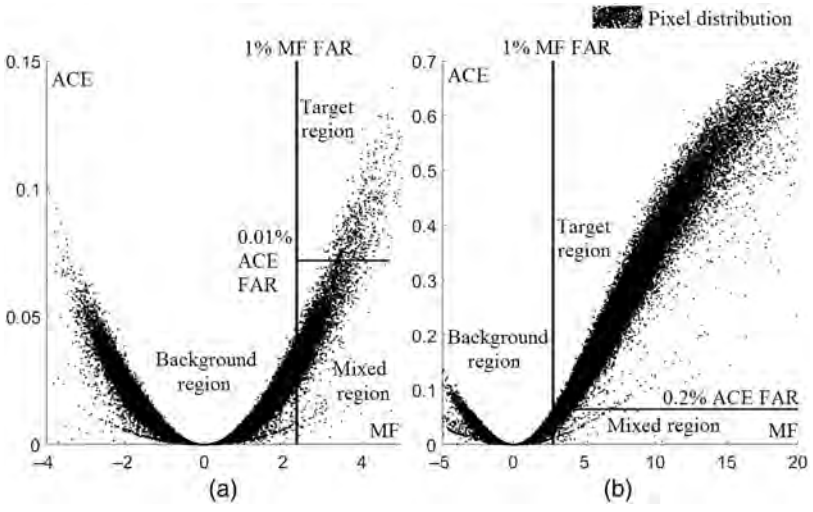

Fig. 18 Background-target separability (a) before and (b) after applying the hybrid method.

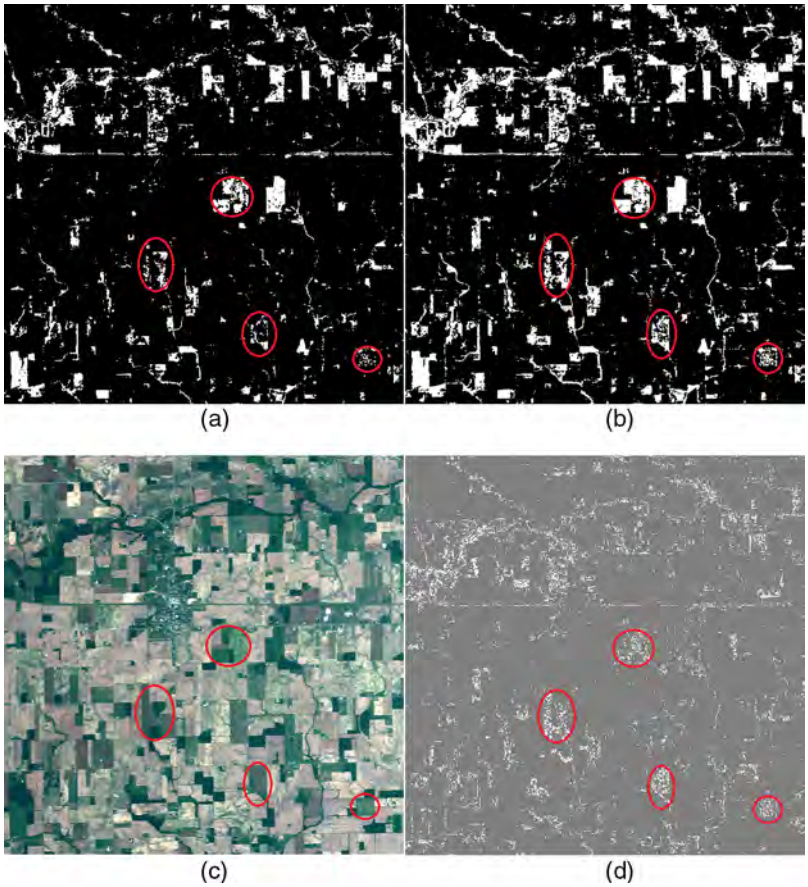

Fig. 19 The detection results of (a) TRDM with 0.1% FAR, (b) the hybrid method with 0.1% FAR, (c) a pseudocolor image of dataset 2, and (d) an image of the differences between panels (b) and (a).

The regions circled in red contained LATs (i.e., a mixture of vegetation and soil). The hybrid method could detect more LATs than could the TRDM method.

5.3.2 *Dataset 3*

The Pavia University image was used to evaluate the experiment of the hybrid detectors in real scenarios, with the Meadow as the target. In evaluating the spectra acquired from the hybrid method, as shown in Table 5, sp13 was the best spectrum according to the terminal conditions.

Table 5 Evaluation of spectra for dataset 3.

Reference spectrum	sp	sp1	sp2	sp3	sp4	sp5	sp6	sp7
Target detected	1538	4198	6265	8488	9449	10304	10976	12193
Max (MF)	5.7	7.2	7.9	8.5	8.7	8.9	9	9.2
Angle	72.05	58.99	51.18	44.58	40.72	37.71	34.26	30.30
Reference spectrum	sp8	sp9	sp10	sp11	sp12	sp13	sp14	
Target detected	13642	15035	16144	17158	17708	18433	18737	
Max (MF)	9.5	9.7	9.9	10.6	11	11.3	11.5	
Angle	25.17	18.30	11.18	6.02	2.52	0	/	

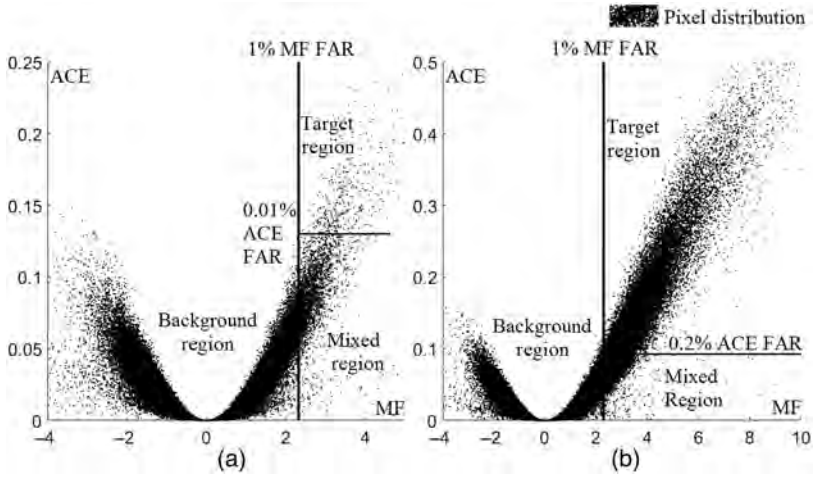

Fig. 20 Background-target separability (a) before and (b) after applying the hybrid method.

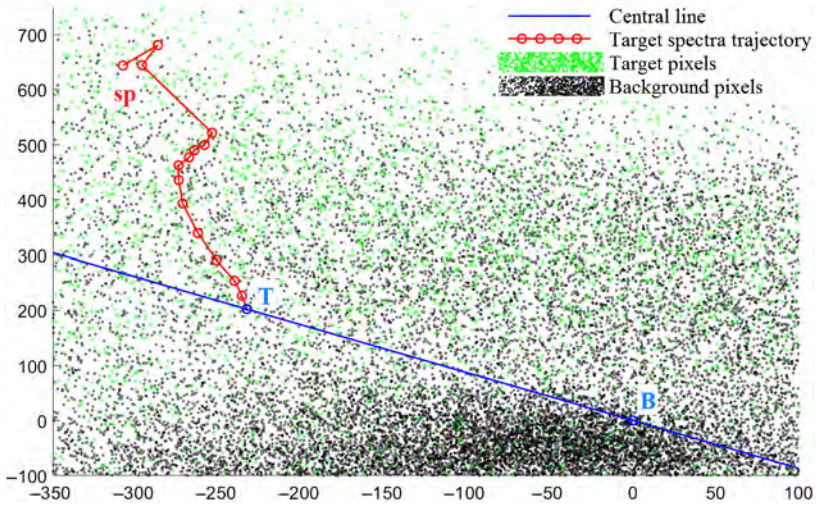

Fig. 21 Improvement in the reference target spectra for dataset 3. *X*-axis and *Y*-axis are fourth and fifth principal components, respectively.

Initial and final background-target separability in the hybrid detection space is shown in Fig. 20. The potential targets escaped from the background region, as shown in Fig. 20(b). Since the ground-truth image was missing, the pixels in the final target region were considered to contain all the targets and the pixels in background region were considered to contain all the background. At this point, centers T and B could be determined and the errors could be minimized. From Fig. 21, one can see that the reference target spectra got closer and closer to the central line as the iterative process proceeded.

Figure 22 shows the detection results when comparing the performance of the TRDM and hybrid methods at 1% FAR. As expected, the hybrid method was superior to the TRDM in detecting the LATs (circled in red).

5.4 *Discussion*

The hybrid detection algorithm developed in this study provides great improvements with regard to its traditional counterparts. In general, the three experiments conducted in this study demonstrated that the hybrid algorithm achieved the best detection performance, as compared with more traditional methods, by gradually improving the reference target spectrum and enhancing target-free background modeling.

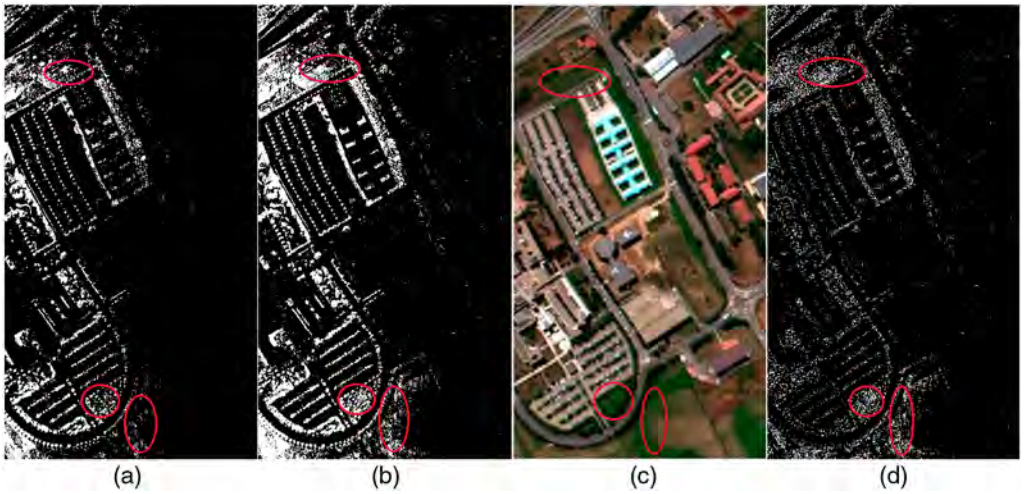

Fig. 22 The detection results of (a) TRDM with 1% FAR, (b) the hybrid method with 1% FAR, (c) the pseudocolor image of dataset 3, and (d) an image of the differences between panels (b) and (a).

While applying the hybrid method, both the number of detected targets inside the hypercone and the average of the top MF scores increased. However, as an updated spectrum got close to the central line, the rate of increase slowed down. When the evaluation metrics reached terminal conditions, the best target spectrum led to optimal detection performance. Furthermore, MF background estimation excluded most of the targets from the background region and yielded better statistics. During the iterative process, the background always was constrained in the background region; furthermore, subpixel targets escaped from the background region, which led to better separability. Among all the algorithms used in the experiments, the hybrid method had the best performance.

6 Conclusions

The principle of hybrid detection space involves first transforming original data into high-dimensional whitened data and then transforming the high-dimensional data into a visualized hybrid detection space. Since background distribution in hybrid detection space is constrained to a small area, targets are easy to separate from the background. In the high-dimensional whitened-data space, any targets of a specific material should follow some distribution principles inside its detection hypercone. This provided a good opportunity to differentiate the target of interest from the background and other abnormalities. The essence of the hybrid method involves finely adjusting the direction of the hypercone, based on target distribution principles, and allowing the hypercone to cover the maximum number of targets.

Because MF and ACE are simple algorithms, it is possible to have real-time processing. The calculation time for six iterations of the hybrid method was 377 s, while the calculation time for the traditional method using N-FINDR endmember extraction was 395 s, both running in MATLAB™ R2016a with i7-4790s CPU and 8GB RAM. In general, the hybrid method did not increase the computational cost.

In our future work, we will try to combine the spatial information of HSI to further improve the detection performance of the hybrid detection algorithm.

Acknowledgments

This research was supported in part by the Nevada EPSCoR program, NSF Award No. EPS-IIA-1301726. The authors would like to acknowledge the National Science Foundation, the Roy & Helen Kelsall Engineering Scholarship, and UNLV's Graduate Access Grant for financial

support on this research. The authors also would like to thank NASA/JPL and the California Institute of Technology as well as the University of the Basque Country in Spain for providing the HSI datasets used in the experiments. Finally, the authors would like to thank Ms. Meagan Madariaga-Hopkins, Mr. Shahab Tayeb, and Mrs. Julie Longo for their help in reviewing this manuscript.

References

1. Y. Choi, E. Sharifahmadian, and S. Latifi, "Performance analysis of contourlet-based hyperspectral image fusion methods," *Int. J. Inf. Theory* **2**(1), 1–14 (2013).
2. M. E. Winter, "N-FINDR: an algorithm for fast autonomous spectral end-member determination in hyperspectral data," *Proc. SPIE* **3753**, 266–275 (1999).
3. F. A. Kruse et al., "The spectral image processing system (SIPS)—interactive visualization and analysis of imaging spectrometer data," *Remote Sens. Environ.* **44**(2–3), 145–163 (1993).
4. W. Li, Q. Du, and B. Zhang, "Combined sparse and collaborative representation for hyperspectral target detection," *Pattern Recognit.* **48**(12), 3904–3916 (2015).
5. F. C. Robey et al., "A CFAR adaptive matched filter detector," *IEEE Trans. Aerosp. Electron. Syst.* **28**(1), 208–216 (1992).
6. E. Conte, M. Lops, and G. Ricci, "Asymptotically optimum radar detection in compound-Gaussian clutter," *IEEE Trans. Aerosp. Electron. Syst.* **31**(2), 617–625 (1995).
7. S. Yang and Z. Shi, "SparseCEM and SparseACE for hyperspectral image target detection," *IEEE Geosci. Remote Sens. Lett.* **11**(12), 2135–2139 (2014).
8. N. M. Nasrabadi, "Hyperspectral target detection: an overview of current and future challenges," *IEEE Signal Process. Mag.* **31**(1), 34–44 (2014).
9. C. E. Davidson and A. Ben-David, "On the use of covariance and correlation matrices in hyperspectral detection," in *IEEE Applied Imagery Pattern Recognition Workshop (AIPR)*, pp. 1–6 (2011).
10. D. Manolakis et al., "Detection algorithms in hyperspectral imaging systems: an overview of practical algorithms," *IEEE Signal Process. Mag.* **31**(1), 24–33 (2014).
11. D. Manolakis et al., "The remarkable success of adaptive cosine estimator in hyperspectral target detection," *Proc. SPIE* **8743**, 874302 (2013).
12. S. Matteoli, M. Diani, and J. Theiler, "An overview of background modeling for detection of targets and anomalies in hyperspectral remotely sensed imagery," *IEEE J. Sel. Top. Appl. Earth Obs. Remote Sens.* **7**(6), 2317–2336 (2014).
13. Q. Guo et al., "Weighted-RXD and linear filter-based RXD: improving background statistics estimation for anomaly detection in hyperspectral imagery," *IEEE J. Sel. Top. Appl. Earth Obs. Remote Sens.* **7**(6), 2351–2366 (2014).
14. B. Pan, Z. Shi, and X. Xu, "MugNet: deep learning for hyperspectral image classification using limited samples," *ISPRS J. Photogramm. Remote Sens.*, in press (2017).
15. B. Pan, Z. Shi, and X. Xu, "R-VCANet: a new deep-learning-based hyperspectral image classification method," *IEEE J. Sel. Top. Appl. Earth Obs. Remote Sens.* **10**(5), 1975–1986 (2017).
16. "AVIRIS-airborne visible/infrared imaging spectrometer," 2017, https://aviris.jpl.nasa.gov/ (24 April 2017).
17. J. B. Adams, M. O. Smith, and P. E. Johnson, "Spectral mixture modeling: a new analysis of rock and soil types at the Viking lander 1 site," *J. Geophys. Res.* **91**(B8), 8098–8112 (1986).
18. J. Shlens "A tutorial on principal component analysis," arXiv:1404.1100 (2014).
19. R. E. Roger and J. F. Arnold, "Reliably estimating the noise in AVIRIS hyperspectral images," *Int. J. Remote Sens.* **17**(10), 1951–1962 (1996).
20. "Hyperspectral remote sensing scenes," 2017, http://www.ehu.eus/ccwintco/index.php?title=Hyperspectral_Remote_Sensing_Scenes (24 April 2017).
21. M. A. Veganzones et al., "Hyperspectral image segmentation using a new spectral unmixing-based binary partition tree representation," *IEEE Trans. Image Process.* **23**(8), 3574–3589 (2014).

Ruixing Li is currently pursuing his MS degree in electrical engineering at the University of Nevada, Las Vegas, United States. His research interests include hyperspectral image analysis, pattern recognition, and data compression.

Shahram Latifi, an IEEE fellow, received his MS degree and PhD in electrical and computer engineering from Louisiana State University, Baton Rouge, in 1986 and 1989, respectively. He is currently a professor of electrical engineering and director of the Center for Information and Communication Technology (CICT) at the University of Nevada, Las Vegas. He is also a registered professional engineer in the state of Nevada.